Static and dynamic correlations in water at hydrophobic interfaces

Jeetain Mittal and Gerhard Hummer[1]

Laboratory of Chemical Physics, National Institute of Diabetes and Digestive and Kidney Diseases, National Institutes of Health, Bethesda, MD 20892-0520

Edited by Hans C. Andersen, Stanford University, Stanford, CA, and approved October 29, 2008 (received for review September 10, 2008)

We study the static and dynamic properties of the water-density fluctuations in the interface of large nonpolar solutes. With the help of extensive molecular dynamics simulations of TIP4P water near smooth spherical solutes, we show that for large solutes, the interfacial density profile is broadened by capillary waves. For purely repulsive solutes, the squared width of the interface increases linearly with the logarithm of the solute size, as predicted by capillary-wave theory. The apparent interfacial tension extracted from the slope agrees with that of a free liquid–vapor interface. The characteristic length of local density fluctuations is ≈0.5 nm, measured along the arc, again consistent with that of a free liquid–vapor interface. Probed locally, the interfacial density fluctuations exhibit large variances that exceed those expected for an ideal gas. Qualitatively consistent with theories of the free liquid–vapor interface, we find that the water interface near large and strongly nonpolar solutes is flickering, broadened by capillary-wave fluctuations. These fluctuations result in transitions between locally wet and dry regions that are slow on a molecular time scale.

capillary waves | drying transition | hydrophobic effect | surface tension

The hydration structure and thermodynamics of simple nonpolar solutes in water is central to a molecular understanding of many biological self-assembly processes, including protein folding and the formation of lipid membranes (1–4). To understand the water-induced conformational changes in biopolymers that lead to functional structures, it is critical to study not only the effects of water on these molecules but also the reverse, i.e., the modified behavior of water in the vicinity of these molecules. To avoid the inherent chemical and structural complexities of present in biological molecules, it is instructive to consider model systems with tunable degrees of freedom. Arguably the simplest such model system is a smooth spherical particle immersed in a water bath (5–18). Such a rudimentary solute model captures two key factors in solvation, the size of the solute and the strength of its interactions with water.

Small, methane-sized solutes are accommodated by water with only minor disruptions of the bulk hydrogen-bond network. The resulting small-solute hydration thermodynamics has been predicted successfully by approaches that take into account the molecular-scale density fluctuations in bulk water, including scaled-particle theory (5, 19) (see ref. 20 for a recent review), Pratt–Chandler theory (8), the Gaussian field model (21), an information theory model (22), and Lum–Chandler–Weeks (LCW) theory (23). With the addition of a large repulsive solute, it becomes impossible for water molecules to maintain their bulk hydrogen-bond structure (24), which also affects the wetting behavior. At ambient conditions the contact theorem predicts a near-zero water density at a flat hard wall (5). Based on this rigorous limit and an interpolation formula, Stillinger anticipated that the water molecules will move away from an extended hydrophobic surface and form a depleted density region near such a surface akin to a water–vapor interface (5). LCW theory (23) provides a statistical-mechanical framework to describe the structure and thermodynamics of such inhomogeneous fluids near phase coexistence, and successfully produces a cross-over in the hydration thermodynamics from a small-length-scale to a large-length-scale dependence (4). In particular, LCW theory predicts that the free energy of hydration scales linearly or superlinearly with solute volume for small solutes but sublinearly, or proportional to solute surface area, for large solutes (11, 13, 23).

Underlying this qualitative change in solvation thermodynamics is the so-called "drying" transition, i.e., the formation of a vapor-like layer near extended hydrophobic surfaces. Examples of drying-induced phenomena include the hydrophobic collapse of a polymer chain (25–27), dewetting-induced attractive interactions studied in detail by Berne, Zhou, and coworkers in the collapse of multidomain proteins and hydrophobic particles (28–30), and large hydrodynamic slip lengths at the solid–water interface (31–33).

Notwithstanding many recent advances toward a consistent picture of water near hydrophobic interfaces, our understanding of microscopic fluctuations at these interfaces is far from clear. Is the interface formed by low-density water, gradually thinning out toward the solute, or is there a sharp transition between a high-density bulk-like phase and a thin vapor-like layer, with the location of the interface wrinkled by capillary waves? What are the length scales and time scales associated with the density fluctuations near the solid surface, as compared with bulk and the planar liquid–vapor interface? How do these properties change with the strength of the solute–water interactions? Here, we try to provide answers to these questions by using molecular dynamics (MD) simulations of a simple model system of a spherical solute in water.

The article is organized as follows. We first study the interfacial density profile and show that its width scales linearly with the logarithm of the solute size for purely repulsive solutes. The apparent surface tension extracted from the slope is shown to agree with that of a liquid–vapor interface. We then probe the local density fluctuations in the interface and show that near large and purely repulsive solutes, the variance of these fluctuations exceeds those expected for an ideal gas. Together the results support the model of a "flickering" water interface near strongly hydrophobic solutes, similar to free liquid–vapor interfaces (34), with dry and wet patches whose relative populations change as a function of solute size.

Results and Discussion

Capillary-Wave Model of Solute–Water Interface. With the help of extensive MD simulations, we explored the static and dynamic correlations of water in nonpolar interfaces. Purely repulsive solutes (RS) and weakly attractive solutes (AS1 and AS2; see *Models and Methods*) up to 4.5 nm in diameter were simulated in water at ambient conditions. From these simulations, we have

Author contributions: J.M. and G.H. designed research, performed research, analyzed data, and wrote the paper.

The authors declare no conflict of interest.

This article is a PNAS Direct Submission.

[1]To whom correspondence should be addressed. E-mail: gerhard.hummer@nih.gov.

This article contains supporting information online at www.pnas.org/cgi/content/full/0809029105/DCSupplemental.

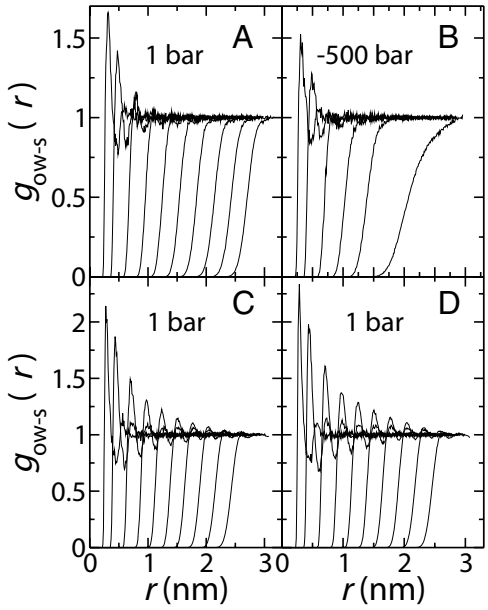

Fig. 1. Radial distribution functions $g_{ow\text{-}s}(r)$ of water oxygen around solutes of diameters σ_s = 0.2, 0.5 1.0, 1.5, 2.0, 2.5, 3.0, 3.5, 4.0, 4.5 nm (from left to right). (*A*) Repulsive solutes RS at 1 bar pressure. (*B*) Repulsive solutes RS at −500 bar. No results are shown for large solutes, $\sigma_s \geq 2.5$ nm, because of cavitation. (*C*) Attractive solutes AS1 at 1 bar. (*D*) Attractive solutes AS2 at 1 bar.

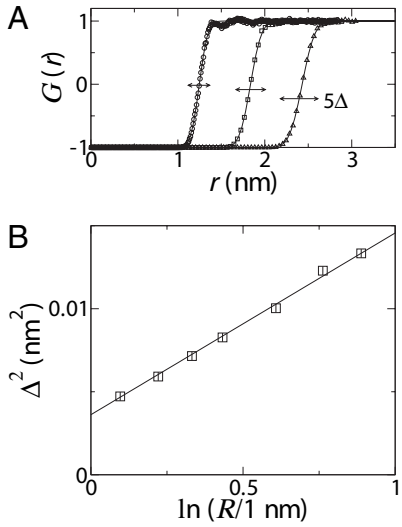

Fig. 2. Interfacial width. (*A*) Scaled density profiles $G(r)$ (symbols; σ_s = 2.0, 3.0, 4.0 nm from left to right) and fits of Eq. **2** (lines), with arrows indicating 5Δ. (*B*) Interfacial width Δ^2 versus the logarithm of the apparent solute size ln(R/1 nm). Simulation data are shown as symbols, together with a linear fit.

determined average solvation structures, the fluctuation-induced broadening of the interface, and the relation between broadening and the interfacial tension as well as the static and dynamic properties of fluctuations in the local water density near the interface.

The radial distribution functions $g_{ow\text{-}s}(r)$ of water oxygen around the solute show a qualitative change in interfacial character from a "wet" to a "dry" interface (Fig. 1). Consistent with earlier studies (9, 11, 13), the water density at contact gradually decreases with increasing solute size. For purely repulsive solutes with diameters σ_s that exceed a critical radius $\sigma_s^c/2 \approx 1$ nm, the contact peak in $g_{ow\text{-}s}(r)$ is entirely absent, and the density profile assumes the sigmoidal shape of a flat liquid–vapor interface. This transition from a wet (peaked) to a dry (sigmoidal) interface, as inferred from $g_{ow\text{-}s}$ at contact, is akin to the small-to-large length-scale cross-over from a solute-volume dependence of the solvation chemical potential to an area dependence (11, 23). Rajamani *et al.* (17) showed that this cross-over moves toward even smaller length scales if the solvent is under hydrostatic tension. Consistent with this previous observation, we find here a smaller σ_s^c for systems under negative pressures (Fig. 1*B*). In contrast, for solutes AS1 and AS2 with attractive solute–solvent interactions $g_{ow\text{-}s}(r)$ remains structured to larger solute sizes (Fig. 1 *C* and *D*).

As shown in Fig. 1, the interfacial density profiles assume similar sigmoidal shapes for large repulsive solutes ($\sigma_s > \sigma_s^c$). However, we find that with increasing solute size, the interfaces become wider (Fig. 1) and recede from the solute for both repulsive and attractive solutes, as compared with the interface locations expected for an ideal gas [supporting information (SI) Fig. S1]. This broadening of the solute–water interface may be a result of the perturbations imposed by the capillary waves to an intrinsic interfacial density profile (35–38). In capillary-wave theory, the interface is treated as a 2-dimensional surface whose fluctuations are Boltzmann-weighted according to the reversible work against a surface tension (35). For a spherical droplet (and by analogy for a bubble, if one ignores issues of mass conservation), the square of the interfacial width Δ^2 is predicted to grow linearly with the logarithm of the radius R (39),

$$\Delta^2 = \Delta_0^2 + \frac{k_B T}{2\pi\gamma} \ln\left(\frac{R}{B_0}\right), \qquad [1]$$

where Δ_0^2 accounts for the intrinsic width, k_B is the Boltzmann constant, T the temperature, γ the apparent interfacial tension, and B_0 a short wavelength cutoff, set effectively by the molecular size.

To determine the width of the interfaces, we fit an error function (40) to the scaled interfacial density profiles

$$G(r) \equiv 2g_{ow\text{-}s}(r) - 1 \approx \mathrm{erf}\left(\frac{r-R}{2^{1/2}\Delta}\right), \qquad [2]$$

as shown in Fig. 2*A*, with R defining an apparent solute size by the midpoint of the solute–water interface. The total interfacial width is then given by $\Delta^2 = \int(r-R)^2 G'(r)dr / \int G'(r)dr$, with $G'(r) = dG/dr$, where the integrals extend over the interfacial region, and curvature corrections are ignored (39).

As shown in Fig. 2*B*, the square of the interfacial width, Δ^2, indeed grows linearly with the logarithm of the apparent solute size, ln R, over the entire range of dry solutes, $1.5 \leq \sigma_s < 4.5$ nm. From the slope of a linear fit (37) of Δ^2 to ln R according to Eq. **1**, we obtain a numerical estimate of the apparent interfacial tension, γ = 60 mN/m. Notably, the surface tension for a planar liquid–vapor interface of TIP4P water was calculated as 54.7 ± 2 mN/m by using the pressure tensor (41) and 53.6 ± 3 mN/m by the capillary-wave method (42). As shown in Fig. S2, the apparent γ from Eq. **1** is slightly changed if we perturbatively correct the interfacial density profile for the broadening induced by the softened water repulsion of large solutes. We further note that the theory, without modifications, is applicable only to a dry solute, for which the solute–water interface can fluctuate freely. The interfacial profiles of the attractive solutes are steeper than those of the purely repulsive solutes (Fig. 1) because the attractive interactions effectively pull in the solvent interface. Overall, the agreement between the apparent surface tension calculated here and the liquid–vapor surface tension provides

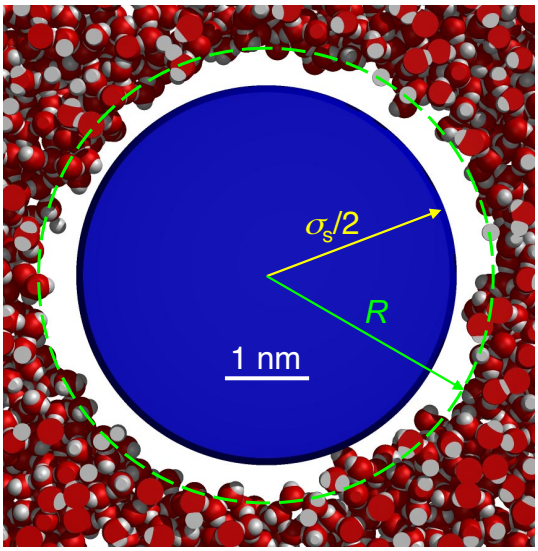

Fig. 3. Snapshot of the solute–water interface for a purely repulsive solute (blue) with $\sigma_s = 4.5$ nm at ambient conditions. Water molecules are shown in red (oxygen) and white (hydrogen). The dashed green circle indicates the apparent solute size R, as determined by fitting of an error function to the density profile, Eq. **2**.

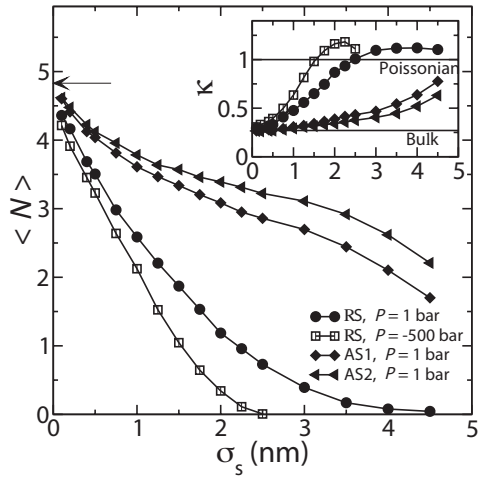

Fig. 4. Average number of water oxygen atoms $\langle N \rangle$ within a probe volume of diameter 0.33 nm placed in contact with the solute as a function of solute size σ_s. The arrow indicates the bulk value for $\langle N \rangle$. (*Inset*) Normalized variance $\kappa = (\langle N^2 \rangle - \langle N \rangle^2)/\langle N \rangle$ as a function of solute size σ_s. Horizontal lines indicate the bulk value for κ, and $\kappa = 1$ for Poissonian statistics.

quantitative support for the presence of a water–vapor interface around a dewetted nonpolar solute.

Density Fluctuations in the Interface. Capillary-wave theory allows us to quantify the fluctuations in the fluid density averaged over the entire interface in terms of a macroscopic surface tension. To gain a microscopic understanding, we probe the local density fluctuations in the interface. A snapshot of the interface around a large repulsive solute is shown in Fig. 3. The cut through the simulation system shows that the fluid phase around the solute remains dense, without any apparent dilution into a low-density vapor-like region. The distance of the dense fluid phase from the solute varies considerably over the solute surface, touching the solute in fingerlike protrusions of a few densely packed water molecules in some places, and receding from the solute in others. Fig. 3 suggests a flickering interface, broadened by the capillary-wave fluctuations underlying Eq. **1**, consistent with the theory of Weeks for liquid–vapor interfaces (34).

To quantify the interfacial density fluctuations, we coarse-grain the local water density over a molecular length scale. Specifically, we determine the fluctuations in the water occupancy numbers in methane-sized spherical probe volumes of $\sigma_p = 0.33$-nm diameter. These probes are placed either at the center of the interface at a distance R from the solute, or in contact with the solute, with their centers separated by a distance $(\sigma_s^{eff} + \sigma_p)/2$, where the effective solute diameter σ_s^{eff} is defined so that $V_{rep}(r = \sigma^{eff}) = k_BT$ (43). V_{rep} is the repulsive part of the solute-water potential, which for attractive solutes is obtained from a Weeks–Chandler–Andersen separation (44).

Fig. 4 shows the average number of water oxygen atoms $\langle N \rangle$ inside the probe volumes for repulsive (RS) as well as attractive (AS1, AS2) solutes. In all cases, the average water density in the interface decreases as the solute size is increased. For purely repulsive solutes, water at contact almost completely disappears for solute diameters >4 and >2.5 nm at 1- and −500-bar pressure, respectively. For the attractive solutes at ambient pressures, the density drop is less pronounced and occurs in steps, the first at $\sigma_s \approx 1$ nm being associated with the reduction in the contact peak of $g_{ow\text{-}s}(r)$, and the second at $\sigma_s > 3$ nm with interfacial broadening (Fig. 1) and the receding interface (Fig. S1). However, for attractive solutes, $\langle N \rangle$ does not drop to zero on the solute size range studied, i.e., the interface remains at least partially wet up to $\sigma_s = 4.5$ nm.

The variance in the water density fluctuations exhibits an even more striking behavior. The *Inset* in Fig. 4 shows the variance in the occupancy number N normalized by its mean value, $(\langle N^2 \rangle - \langle N \rangle^2)/\langle N \rangle$, as a function of the solute diameter σ_s for the different solute types. In the macroscopic limit, the ratio of variance and average approaches $\rho k_BT\, \chi_T$, where χ_T is the isothermal compressibility. The horizontal lines in Fig. 4 indicate the 2 limiting cases of fluctuations for a 0.33-nm-diameter probe volume in bulk water, and for the Poissonian statistics of an ideal gas. As the size of the repulsive solutes increases, κ rises to values ≈4 times those in bulk water. This large variance in the density fluctuations suggests that water near large hydrophobic solutes is more compressible, owing to fluctuations between locally dry and wet states and consistent with a large drop in $\langle N \rangle$ at −500-bar pressure (Fig. 4). Large compressibility was previously reported for water confined between hydrophobic plates (45).

Remarkably, for large repulsive solutes, κ even exceeds the ideal-gas limit of 1. This super-Poissonian statistics (46) suggests that a weak clustering may contribute to the density fluctuations, consistent with the structures seen in the simulation snapshot Fig. 3 and the capillary-wave theory. Note, however, that the probabilities $P(N)$ are not bimodal (Fig. S3). The peak in κ (Fig. 4 *Inset*) is also reminiscent of the drying transitions between extended hydrophobic surfaces (47) and in long nanopores (48). We note that for a planar TIP4P liquid–vapor interface, we find $\kappa \approx 1$ at the center, and $\kappa > 1$ in the interfacial region on the vapor side (data not shown).

Range of Interfacial Density Fluctuations. The spatial range of the density fluctuations in the interface of the repulsive solutes can be determined from distance-dependent static cross-correlation functions of the coarse-grained density. Fig. 5 shows the normalized correlation coefficient $C_{12} = (\langle N_1 N_2 \rangle - \langle N \rangle^2)/(\langle N^2 \rangle - \langle N \rangle^2)$ where N_1 and N_2 are the occupancy numbers of 2 spherical probe volumes of diameter 0.33 nm placed in the solute–water interface, with $\langle N \rangle = \langle N_i \rangle$, and $\langle N^2 \rangle = \langle N_i^2 \rangle$. C_{12} is plotted as a function of the distance R along the arc connecting the centers of the 2 probe volumes. We find that C_{12} decays approximately exponentially with the arc length. For probes placed at the center of the interface at a distance R from the solute, we define the

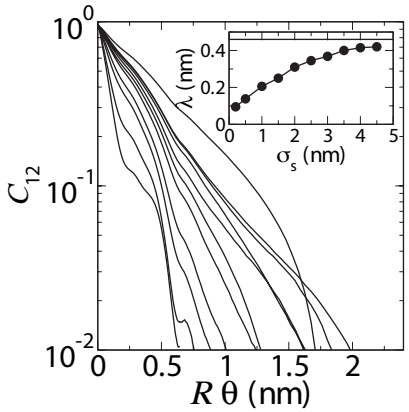

Fig. 5. Static cross-correlation function C_{12} of the interfacial water density as a function of arc distance (solid lines; σ_s from 0.2 to 4.5 nm, from left to right as in Fig. 1) and at the planar liquid–vapor interface (dashed line). C_{12} is defined as the normalized correlation coefficient of the water oxygen occupancy numbers in 2 spherical probe volumes of 0.33-nm diameter, with their centers at a distance R from the purely repulsive solute and separated by an arc length $s = R\theta$. For a planar liquid–vapor interface, s is the distance between the 2 probes. The *Inset* shows the correlation length λ as a function of the solute size (solid circles joined by a line) and for a planar liquid–vapor interface (dashed line).

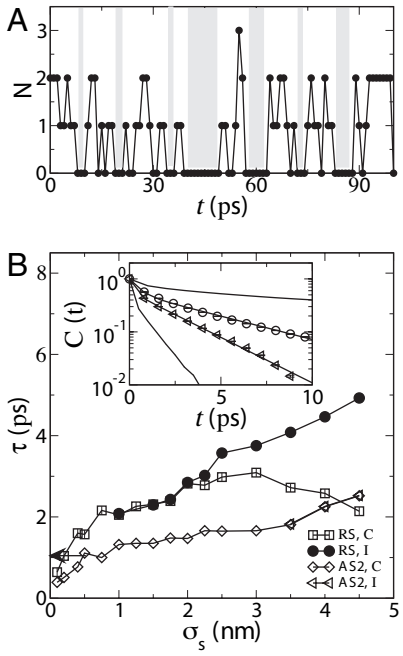

Fig. 6. Temporal correlations of fluctuations in the solute–water interface at 1 bar. (*A*) Representative time series $N(t)$ of the number of water oxygen atoms within a 0.33-nm diameter probe volume placed in contact with a σ_s = 2.5-nm solute. Shaded rectangles indicate transient locally dry states. (*B*) Slow relaxation time τ extracted from a biexponential fit to the autocorrelation functions $C(t)$ of $N(t)$, for probe volumes in contact with the solute (dashed lines) and at the center of the interface (solid lines), with filled and open symbols for the purely repulsive RS solute and the attractive AS2 solute, respectively. The arrow indicates the bulk value. (*Inset*) Autocorrelation function $C(t)$ for a probe in the interface of the σ_s = 4.5 nm repulsive solute (circles), attractive solute (triangles), in the bulk (solid line), and at the planar liquid–vapor interface (dashed line).

correlation length λ as the distance where C_{12} drops to e^{-1}. The resulting λ values range from 0.1 to ≈0.45 nm for σ_s between 0.1 and 4.5 nm (Fig. 5). Similar values were obtained for probes placed in contact with the solute and for probes placed in a planar liquid–vapor interface of TIP4P water (Fig. 5 *Inset*; note that we expect a system-size-dependent λ also for the flat liquid–vapor interface).

Dynamics of Interfacial Density Fluctuations. To probe the dynamics of the density fluctuations near dewetted solutes, we follow the time dependence of the water occupancy in probe volumes kept at a fixed location with respect to the solute. Fig. 6*A* shows a representative time series of N for a 0.33-nm-diameter probe in contact with a σ_s = 2.5-nm solute. We observe intermittent dry periods (with $n = 0$) of up to ≈5-ps duration, indicated by gray shading in the time series, separated by longer wet periods with $N \geq 1$. We note that $n = 0$ is visited both during dry and wet periods, indicating that N is not a good order parameter to probe transitions between the locally wet and dry states. Indeed, the normalized autocorrelation functions $C(t)$ of $N(t)$ show biexponential behavior (Fig. 6*B Inset*). We find that the time constant of the fast relaxation does not change appreciably with solute size (data not shown), and associate this fast phase with water molecules moving in and out of the probe volume in the locally wet state. In contrast, the slow relaxation time slows down as the solute size is increased, and we associate it with transitions between locally wet and dry states (Fig. 6*B*). For probes placed in the interface (at a distance R), τ increases monotonically with σ_s. Qualitatively similar behavior is obtained for attractive solutes, but with a shorter relaxation time τ dominated by the shorter lifetime of locally dry states. For probes placed at the center of a planar liquid–vapor interface (simulated under periodic boundary conditions), we obtain a correlation time of ≈13 ps (Fig. 6*B Inset*). This somewhat slower relaxation time is qualitatively consistent with the gradual increase of τ with solute size seen in Fig. 6*B*. However, a quantitative comparison would require infinite system-size limits for both the solute–water and liquid–vapor interfacial systems. In contrast to probes placed at the center of the interface, for probes at contact with the largest purely repulsive solutes, τ levels out, being dominated by the short lifetime of locally wet states as the average occupancy $\langle N \rangle$ approaches zero.

Concluding Remarks

Water "evaporating" from nonpolar confinement has been observed in a number of simulation studies and has been unequivocally demonstrated in at least 1 experiment probing the hydration of a protein cavity (49). Simulation examples of such confinement-induced drying (50) range from nanotubes (51) to plates (28, 45, 52–59) and the interfaces between proteins (30, 60) to collapsing polymers (25–27). Associated with these surface-induced drying transitions are nanometer-scale fluctuations in the local water density (27), resulting in detectable locally liquid-like and vapor-like phases. Here, we have probed the more subtle fluctuations in the water density near convex-shaped nonpolar solutes. We find that these fluctuations occur on smaller, subnanometer-length scales and do not result in the dramatic and clearly detectable creation of large voids. Nevertheless, these density fluctuations exhibit the signatures expected for liquid–vapor interfaces.

From the static and dynamic correlations of interfacial density fluctuations, the picture of a rough and flickering interface emerges. The sigmoidal-shaped density profiles are broadened by capillary-wave fluctuations that roughen an otherwise sharp spatial transition between the dense liquid and the molecularly thin vapor-like region surrounding the solute. Drying is enhanced by putting the fluid under tension (by applying negative pressure). In contrast, attractive solute–water interactions are found to favor a wet interface. Nonetheless, the interface recedes

from large attractive solutes (Fig. S1). This observation suggests that weak attractions shift the drying transition but do not fundamentally alter the liquid–vapor-like character of the interface, consistent with recent simulation studies (61).

Quantitative demonstrations of drying at nonpolar interfaces have built on the predicted surface-area dependence of the solvation free energy (5, 23), with a proportionality constant comparable with the macroscopic liquid–vapor surface tension. However, such comparisons are complicated, for instance, by the necessary corrections for the solute curvature, involving Tolman's length (62). Here, we directly relate the microscopic structure of the solute–water interface to the interfacial tension, a formalism that was previously applied to liquid–vapor interfaces (42). Under the assumption of dewetting at the interface, capillary-wave theory predicts that the square of the interfacial width should grow linearly with the logarithm of the solute size. Indeed, that is what we observed here. Moreover, as predicted by capillary-wave theory, we find that the apparent surface tension extracted from the slope agrees nearly quantitatively with that calculated for a planar liquid–vapor interface. Put together, these observations provide a demonstration of the vapor-like region near large nonpolar solutes in water, as anticipated by Stillinger (5) and obtained as a central result from the theory of Lum, Chandler, and Weeks (4, 23).

Models and Methods

MD simulations are performed with GROMACS 3.3.1 (63). Temperature and pressure are held constant at 300 K and either 1 or −500 bar by using a Langevin thermostat and Berendsen barostat (64), respectively, each with time constants of 1 ps. The solute and water oxygen atoms interact via a potential $V(r) = 4[\varepsilon_{12}(\sigma/r)^{12} - \varepsilon_6(\sigma/r)^6]$, where r is the radial distance. Solute–water parameters are obtained by Lorentz–Berthelot mixing, with solute–solute parameters of $\varepsilon_{12}^{s} = 1$ kJ/mol and $\varepsilon_6^{s} = 0$ (purely repulsive solute RS), $\varepsilon_{12}^{s} = \varepsilon_6^{s} = 2$ kJ/mol (attractive solute AS1), and $\varepsilon_{12}^{s} = \varepsilon_6^{s} = 4$ kJ/mol (attractive solute AS2). The solute diameter σ_s is varied between 0.1 and 4.5 nm. The solutes are immersed in a periodically replicated box of $N_W = 6{,}000$ TIP4P water molecules (65). We use $N_W = 6{,}000$ TIP4P water molecules to simulate a planar liquid–vapor interface in a periodic box of dimensions $5.6723 \times 5.6723 \times 20$ nm^3. Electrostatic interactions are calculated with particle-mesh Ewald summation (66). The simulation time step is 2 fs. After equilibration, ≈1,500 snapshots of the system are saved at 0.4-ps intervals for analysis. In close agreement with experiment (23), liquid TIP4P water at $P = 1$ bar pressure and 300 K temperature is near coexistence with its vapor, with the free energies per particle in the gas and liquid differing by $\mu_g - \mu_l \approx P/\rho_l \approx 1.8 \times 10^{-3}$ kJ/mol, where ρ_l is the liquid density.

We note that the estimated interfacial widths change slightly if we perturbatively correct for the effects of the softening of the solute–water interactions with increasing solute size, $g_{ow\text{-}s}^{corr}(r) \approx \exp[-(V_{ref}(r) - V(r))/k_BT]g_{ow\text{-}s}(r)$ (9), where $V(r)$ is the solute–water interaction potential, and $V_{ref}(r)$ is a reference solute–water interaction potential that does not change shape as the solute size is increased (see Fig. S2).

ACKNOWLEDGMENTS. J.M. thanks Dr. Artur Adib for several helpful discussions and supporting a postdoctoral fellowship during this work. We also thank Dr. Attila Szabo (National Institutes of Health), Dr. Robert Best (University of Cambridge, Cambridge, U.K.), and Sapna Sarupria (Rensselaer Polytechnic Institute, Troy, NY) for pertinent suggestions. This work was supported by the Intramural Research Program of the National Institutes of Health (NIH), National Institute of Diabetes and Digestive and Kidney Diseases. This study used the high-performance computational capabilities of the Biowulf PC/Linux cluster at the NIH (http://biowulf.nih.gov).

1. Kauzmann W (1959) Some factors in the interpretation of protein denaturation. *Adv Protein Chem* 14:1–63.
2. Tanford C (1973) *The Hydrophobic Effect: Formation of Micelles and Biological Membranes* (Wiley, New York).
3. Dill KA (1990) Dominant forces in protein folding. *Biochemistry* 29:7133–7155.
4. Chandler D (2005) Interfaces and the driving force of hydrophobic assembly. *Nature* 437:640–647.
5. Stillinger FH (1973) Structure in aqueous solutions of nonpolar solutes from the standpoint of scaled-particle theory. *J Sol Chem* 2:141–158.
6. Ben-Naim A (1974) *Water and Aqueous Solutions* (Plenum, New York).
7. Franks F (1975) *Water, A Comprehensive Treatise* (Plenum, New York).
8. Pratt LR, Chandler D (1977) Theory of the hydrophobic effect. *J Chem Phys* 67:3683–3704.
9. Hummer G, Garde S (1998) Cavity expulsion and weak dewetting of hydrophobic solutes in water. *Phys Rev Lett* 80:4193–4196.
10. Hummer G, Garde S, García AE, Paulaitis ME, Pratt LR (1998) Hydrophobic effects on a molecular scale. *J Phys Chem B* 102:10469–10482.
11. Huang DM, Geissler PL, Chandler D (2001) Scaling of hydrophobic solvation free energies. *J Phys Chem B* 105:6704–6709.
12. Southall NT, Dill KA, Haymet ADJ (2002) A view of the hydrophobic effect. *J Phys Chem B* 106:521–533.
13. Huang DM, Chandler D (2002) The hydrophobic effect and the influence of solute-solvent attractions. *J Phys Chem B* 106:2047–2053.
14. Ashbaugh HS, Paulaitis ME (2001) Effect of solute size and solute-water attractive interactions on hydration water structure around hydrophobic solutes. *J Am Chem Soc* 123:10721–10728.
15. Ashbaugh HS, Truskett TM, Debenedetti PG (2002) A simple molecular thermodynamic theory of hydrophobic hydration. *J Chem Phys* 116:2907–2921.
16. Paschek D (2004) Temperature dependence of the hydrophobic hydration and interaction of simple solutes: An examination of five popular water models. *J Chem Phys* 120:6674–6690.
17. Rajamani S, Truskett TM, Garde S (2005) Hydrophobic hydration from small to large lengthscales: Understanding and manipulating the crossover. *Proc Natl Acad Sci USA* 102:9475–9480.
18. Buldyrev SV, Kumar P, Debenedetti PG, Rossky PJ, Stanley HE (2007) Water-like solvation thermodynamics in a spherically symmetric solvent model with two characteristic lengths. *Proc Natl Acad Sci USA* 104:20177–20184.
19. Pierotti RA (1976) A scaled particle theory of aqueous and non- aqueous solutions. *Chem Rev* 76:717–726.
20. Ashbaugh HS, Pratt LR (2005) Colloquium: Scaled particle theory and the length scales of hydrophobicity. *Rev Mod Phys* 78:159- 178.
21. Chandler D (1993) Gaussian field model of fluids with an application to polymeric fluids. *Phys Rev E* 48:2898–2905.
22. Hummer G, Garde S, García AE, Pohorille A, Pratt LR (1998) An information theory model of hydrophobic interactions. *Proc Natl Acad Sci USA* 93:8951–8955.
23. Lum K, Chandler D, Weeks JD (1999) Hydrophobicity at small and large length scales. *J Phys Chem B* 103:4570–4577.
24. Lee CY, McCammon JA, Rossky PJ (1984) The structure of liquid water at an extended hydrophobic surface. *J Chem Phys* 80:4448–4455.
25. ten Wolde PR, Chandler D (2002) Drying induced hydrophobic polymer collapse. *Proc Natl Acad Sci USA* 99:6539–6543.
26. Athawale MV, Goel G, Ghosh T, Truskett TM, Garde S (2007) Effects of lengthscales and attractions on the collapse of hydrophobic polymers in water. *Proc Natl Acad Sci USA* 104:733–738.
27. Miller TF, Vanden-Eijnden E, Chandler D (2007) Solvent coarse-graining and the string method applied to the hydrophobic collapse of a hydrated chain. *Proc Natl Acad Sci USA* 104:14559–14564.
28. Wallqvist A, Berne BJ (1995) Computer simulation of hydrophobic hydration forces on stacked plates at short range. *J Phys Chem* 99:2893–2899.
29. Zhou R, Huang X, Margulis CJ, Berne BJ (2004) Hydrophobic collapse in multidomain protein folding. *Science* 305:1605–1609.
30. Liu P, Huang X, Zhou R, Berne BJ (2005) Observation of a dewetting transition in the collapse of the melittin tetramer. *Nature* 437:159–162.
31. Lauga E, Brenner MP, Stone HA (2006) *Handbook of Experimental Fluid Mechanics*, eds Tropea C, Foss J, Yarin A (Springer, New York).
32. Joseph P, *et al.* (2006) Slippage of water past superhydrophobic carbon nanotube forests in microchannels. *Phys Rev Lett* 97:156104.
33. Meyer EE, Rosenberg KJ, Israelachvili J (2006) Recent progress in understanding hydrophobic interactions. *Proc Natl Acad Sci USA* 103:15739–15746.
34. Weeks JD (1977) Structure and thermodynamics of the liquid–vapor interface. *J Chem Phys* 67:3106–3121.
35. Buff FP, Lovett RA, Stillinger FH (1965) Interfacial density profile for fluids in the critical region. *Phys Rev Lett* 15:621–623.
36. Rowlinson JS, Widom B (2003) *Molecular Theory of Capillarity* (Dover, New York).
37. Lacasse MD, Grest GS, Levine AJ (1998) Capillary-wave and chain-length effects at polymer/polymer interfaces. *Phys Rev Lett* 80:309–312.
38. Chowdhary J, Ladanyi BM (2006) Water/hydrocarbon interfaces: Effect of hydrocarbon branching on interfacial/structure. *J Phys Chem B* 110:15442–15453.
39. Henderson JR, Lekner J (1978) Surface oscillations and the surface thickness of classical and quantum droplets. *Mol Phys* 36:781–789.
40. Sides SW, Grest GS, Lacasse MD (1999) Capillary waves at liquid–vapor interfaces: A molecular dynamics simulation. *Phys Rev E* 60:6708–6713.
41. Chen F, Smith PE (2007) Simulated surface tensions of common water models. *J Chem Phys* 126:221101.
42. Ismail AE, Grest GS, Stevens MJ (2006) Capillary waves at the liquid–vapor interface and the surface tension of water. *J Chem Phys* 125:014702.
43. Ben-Amotz D, Stell G (2004) Reformulation of Weeks–Chandler–Andersen perturbation theory directly in terms of a hard-sphere reference system. *J Phys Chem B* 108:6877–6882.
44. Weeks JD, Chandler D, Andersen HC (1971) Role of repulsive forces in forming the equilibrium structure of simple liquids. *J Chem Phys* 55:5422–5423.
45. Giovanbattista N, Rossky PJ, Debenedetti PG (2006) Effect of pressure on the phase behavior and structure of water confined between nanoscale hydrophobic and hydrophilic plates. *Phys Rev E* 73:041604.

46. Kostinski AB, Shaw RA (2001) Scale-dependent droplet clustering in turbulent clouds. *J Fluid Mech* 434:389–398.
47. Choudhury N, Pettitt BM (2007) The dewetting transition and the hydrophobic effect. *J Am Chem Soc* 129:4847–4852.
48. Köfinger J, Hummer G, Dellago C (2008) Macroscopically ordered water in nanopores. *Proc Natl Acad Sci USA* 105:13218–13222.
49. Collins MD, Hummer G, Quillin ML, Matthews BW, Gruner SM (2005) Cooperative water filling of a nonpolar protein cavity observed by high-pressure crystallography and simulation. *Proc Natl Acad Sci USA* 102:16668–16671.
50. Rasaiah JC, Garde S, Hummer G (2008) Water in nonpolar confinement: From nanotubes to proteins and beyond. *Annu Rev Phys Chem* 59:713–740.
51. Hummer G, Rasaiah JC, Noworyta JP (2001) Water conduction through the hydrophobic channel of a carbon nanotube. *Nature* 414:188–190.
52. Luzar A, Leung K (2000) Dynamics of capillary evaporation. I. Effect of morphology of hydrophobic surfaces. *J Chem Phys* 113:5836–5844.
53. Bratko D, Curtis RA, Blanch HW, Prausnitz JM (2001) Interaction between hydrophobic surfaces with metastable intervening liquid. *J Chem Phys* 115:3873–3877.
54. Truskett TM, Debenedetti PG, Torquato S (2001) Thermodynamic implications of confinement for a waterlike fluid. *J Chem Phys* 114:2401–2418.
55. Huang X, Margulis CJ, Berne BJ (2003) Dewetting-induced collapse of hydrophobic particles. *Proc Natl Acad Sci USA* 100:11953–11958.
56. Choudhury N, Pettitt BM (2005) On the mechanism of hydrophobic association of nanoscopic solutes. *J Am Chem Soc* 127:3556–3567.
57. Vaitheeswaran S, Yin H, Rasaiah JC (2005) Water between plates in the presence of an electric field in an open system. *J Phys Chem B* 109:6629–6635.
58. Urbic T, Vlachy V, Dill KA (2006) Confined water: A Mercedes–Benz model study. *J Phys Chem B* 110:4963–4970.
59. Giovanbattista N, Debenedetti PG, Rossky PJ (2007) Hydration behavior under confinement by nanoscale surfaces with patterned hydrophobicity and hydrophilicity. *J Phys Chem C* 111:1323–1332.
60. Giovanbattista N, Lopez CF, Rossky PJ, Debenedetti PG (2008) Hydrophobicity of protein surfaces: Separating geometry from chemistry. *Proc Natl Acad Sci USA* 105:2274–2279.
61. Willard AP and Chandler D (2009) Coarse-grained modeling of the interface between water and heterogeneous surfaces. *Faraday Discuss*, in press, and discussion (http://dx.doi.org/10.1039/b805786a).
62. Rowlinson JS (1994) A drop of liquid. *J Phys Condensed Matter* 6:A1–A8.
63. Lindahl E, Hess B, van der Spoel D (2001) Gromacs 3.0: A package for molecular simulation and trajectory analysis. *J Mol Mod* 7:306–317.
64. Berendsen HJC, Postma JPM, van Gunsteren WF, DiNola A, Haak JR (1984) Molecular dynamics with coupling to an external bath. *J Chem Phys* 81:3684–3690.
65. Jorgensen WL, Madura JD (1985) Temperature and size dependence for Monte Carlo simulations of TIP4P water. *Mol Phys* 56:1381–1392.
66. Darden T, York D, Pedersen L (1993) Particle mesh Ewald: An N-log(N) method for Ewald sums in large systems. *J Chem Phys* 98:10089–10092.